Fatigue performance of additively manufactured meta-biomaterials

The effects of topology and material type

Ahmadi, S. M.; Hedayati, R.; Li, Y.; Lietaert, K.; Tümer, N.; Fatemi, A.; Rans, C. D.; Pouran, B.; Weinans, H.; Zadpoor, A. A.

DOI
10.1016/j.actbio.2017.11.014

Publication date
2018

Document Version
Accepted author manuscript

Published in
Acta Biomaterialia

Citation (APA)
Ahmadi, S. M., Hedayati, R., Li, Y., Lietaert, K., Tümer, N., Fatemi, A., Rans, C. D., Pouran, B., Weinans, H., & Zadpoor, A. A. (2018). Fatigue performance of additively manufactured meta-biomaterials: The effects of topology and material type. *Acta Biomaterialia*, *65*, 292-304. https://doi.org/10.1016/j.actbio.2017.11.014

Original article

Fatigue performance of additively manufactured meta-biomaterials: the effects of topology and material type

S.M. Ahmadi[1,†], R. Hedayati[1,2,†], Y. Li[1], K. Lietaert[3], N.Tümer[1], A. Fatemi[4], C.D. Rans[5], B. Pouran[1,2], H. Weinans[1,2,6], A.A. Zadpoor[1]

[1]*Department of Biomechanical Engineering, Faculty of Mechanical, Maritime, and Materials Engineering, Delft University of Technology (TU Delft), Mekelweg 2, 2628 CD, Delft, The Netherlands*

[2]*Department of Orthopedics, University Medical Center Utrecht, Heidelberglaan100, 3584CX Utrecht, The Netherlands*

[3]*3D Systems−LayerWise NV, Grauwmeer 14, 3001 Leuven, Belgium*

[4]*Mechanical, Industrial and Manufacturing Engineering Department, The University of Toledo, 2801 West Bancroft Street, Toledo, OH 43606, USA*

[5]*Faculty of Aerospace Engineering, Delft University of Technology, 2629 HS Delft, The Netherlands*

[6]*Department of Rheumatology, University Medical Center Utrecht, Heidelberglaan100, 3584CX Utrecht, The Netherlands*

[†]Both authors equally contributed to this work

Abstract

Additive manufacturing (AM) techniques enable fabrication of bone-mimicking meta-biomaterials with unprecedented combinations of topological, mechanical, and mass transport properties. The mechanical performance of AM meta-biomaterials is a direct function of their topological design. It is, however, not clear to what extent the material type is important in determining the fatigue behavior of such biomaterials. We therefore aimed to determine the isolated and modulated effects of topological design and material type on the fatigue response of metallic meta-biomaterials fabricated with selective laser melting. Towards that end, we designed and additively manufactured Co-Cr meta-biomaterials with three types of repeating unit cells and three to four porosities per type of repeating unit cell. The AM meta-biomaterials were then mechanically tested to obtain their normalized S-N curves. The obtained S-N curves of Co-Cr meta-biomaterials were compared to those of meta-biomaterials with same topological designs but made from other materials, i.e. Ti-6Al-4V, tantalum, and pure titanium, available from our previous studies. We found the material type to be far more important than the topological design in determining the normalized fatigue strength of our AM metallic meta-biomaterials. This is the opposite of what we have found for the quasi-static mechanical properties of the same meta-biomaterials. The effects of material type, manufacturing imperfections, and topological design were different in the high and low cycle fatigue regions. That is likely because the cyclic response of meta-biomaterials depends not only on the static and fatigue strengths of the bulk material but also on other factors that may include strut roughness, distribution of the micro-pores created inside the struts during the AM process, and plasticity.

Keywords: Co-Cr; Additive manufacturing; Fatigue behavior; Porous biomaterial.

1. INTRODUCTION

Metamaterials are materials with (unusual) mechanical, physical, or biological properties that result from the topological design of their micro-architecture as well as the type of the material from which they are made. In essence, metamaterials are repetitive structures that are convenient to treat as materials for many applications given the length scale of their micro-architectures. Depending on the physical property of interest, metamaterials are called optical metamaterials [1-4], mechanical metamaterials [5-8], or acoustic metamaterials [9-11]. Meta-biomaterials [12] are a specific class of metamaterials with biomedical applications. As opposed to the other types of metamaterials where only one specific property of the material is of interest, meta-biomaterials are simultaneously designed for several types of properties including mechanical, mass transport, and biological properties [13-17]. Given the importance of topological design in determining the properties of metamaterials, the form-freedom offered by additive manufacturing (AM) techniques is instrumental in realizing meta-biomaterials with arbitrarily complex topologies of the micro-architecture and, thus, unique properties.

Bone-mimicking meta-biomaterials are a special type of such materials that are used either as bone substitutes to expedite bone tissue regeneration or as parts of orthopedic implants to facilitate osseointegration and improve implant longevity. Various properties of bone-mimicking meta-biomaterials need to be simultaneously adjusted for optimal bone tissue regeneration and implants fixation. In this study, however, we are primarily concerned with the mechanical properties in general and the fatigue behavior in particular while focusing on the metallic meta-biomaterials that show high mechanical properties and long fatigue lives. Those biomaterials are often subjected to many cycles of musculoskeletal loads specially when used in load-bearing parts of the skeleton, highlighting the importance of studying their fatigue response. Significant

research has been conducted during the last few years into the fatigue behavior of metallic meta-biomaterials. The major modes of loading in bone-mimicking meta-biomaterials is compression and bending. Given the relative simplicity of compression test setups, the fatigue behavior of meta-biomaterials is usually studied under compression-compression loading when establishing S-N curves [12, 18-22].

Previous studies have shown that the topological design of meta-biomaterials including the geometry of the repeating unit cell and the relative density of the porous structure (i.e. the ratio of the density of the porous structure to the density of the bulk material it is made of: $\mu = {}^{\rho}/_{\rho_s}$) could influence their static [23-27] and fatigue [12, 28] properties. In our previous studies, it was demonstrated that the normalized S-N curves of meta-biomaterials with different relative densities but with the same unit cell and material type are close to each other [22]. The normalized S-N curves are obtained by dividing the levels of stress applied to the meta-biomaterial by its yield stress [12]. The main concerns of the previous studies have been to investigate the effects of the topological characteristics of the porous structure on their fatigue response, and as a result the performance comparisons have been made between porous structures with different topological designs but made from the same bulk materials (e.g. steel [29, 30], magnesium [31, 32], titanium [33-35], Co-Cr [36, 37]). Therefore, it is currently not clear what the effects of material type on the normalized S-N curve are. Moreover, possible modulations between the topological design and material type in determining the fatigue life have not been studied before.

The aim of the current study was to investigate the isolated and modulated effects of topological design and material type on the compressive-compressive fatigue behavior of bone-mimicking metallic meta-biomaterials. Fatigue responses (S-N curves) of meta-biomaterials with different

topological designs made from different materials were needed to systematically address that research question. We therefore determined the compression-compression S-N curves for a large set of different topological designs of bone-mimicking meta-biomaterials made from a Co-Cr alloy. The topological designs included three different types of repeating unit cells and three or four porosities for each type of the repeating unit cell. The generated data was used in combination with the S-N curves available from our previous studies on the fatigue behavior of meta-biomaterials made from Ti-6Al-4V [12, 22], pure titanium [38], and tantalum [39].

2. MATERIALS AND METHODS

2.1. Materials and manufacturing

Meta-biomaterials (Figure 1) with a wide range of relative densities ($0.27 < \mu < 0.42$ for truncated cuboctahedron, $0.29 < \mu < 0.42$ for rhombic dodecahedron, and $0.21 < \mu < 0.41$ for diamond) (Table 1) were AM using a selective laser melting (SLM) machine. The strut sizes of all meta-biomaterials were in the range of $339.8\ \mu m$ to $486.3\ \mu m$ (Table 1). To manufacture the structures, Co-Cr powder conforming to ASTM F75 (Cr 28.5%, Mo 6%) was processed on top of a solid substrate under inert atmosphere. After the manufacturing process, the specimens were removed from the solid substrate using electro discharging machine (EDM). Ultrasonic cleaning was used to remove the powder residues before microstructural, morphological, and mechanical characterizations. All specimens were cylindrical with diameters of 15 mm and lengths of 20 mm. For the meta-biomaterials based on the diamond and truncated cuboctahedron unit cells, four different densities were considered, while for the those based on rhombic dodecahedron, three different densities were designed and AM (Table 1). For each unit cell size and porosity, more than 15 specimens were manufactured. Three of the specimens were used for compressive

static tests (to obtain the yield stress of each structure type) [40] and the rest of the specimens were used for fatigue tests under different stress levels to obtain the S-N curve.

2.2. Topological characterization

Two different techniques, namely micro-computed tomography (μCT) and dry weighing, were used to measure the topological parameters of Co-Cr porous structures including density, strut size, and pore size [40]. In the dry weighing method, the weight of each specimen was measured in atmospheric conditions, and was then divided by the volume of the specimen to obtain the average density. Subsequently, the obtained average density value was divided by the density of the bulk Co-Cr material (i.e. $\rho_s = 8800\, kg/m^3$) to calculate the relative density of each specimen. Archimedes technique was used in combination with dry weighing to measure the volume occupied by the internal pores in the struts.

As for μCT scanning, specimens were scanned using Quantum FX (Perkin Elmer, Waltham, MA, USA). The following parameters were used as a part of the scanning protocol: tube current = 180 μA, tube voltage = 90 kV, scanning time = 3 min, and resolution = 42 μm. Based on the scanned 2D images, 3D geometries were constructed using the algorithms built in the scanner software. The constructed 3D geometries were then exported to Caliper Analyze 11.0 (Perkin Elmer, USA) to regain the 2D images of the specimens. Using ImageJ software, the regions of interest (ROIs) of the 2D images were created and the porosity was calculated. The inverse of porosity was used to calculate the volume occupied by the metallic parts of the porous structure, thus, giving the relative density.

2.3. Microstructural characterization

To observe the microstructural features of the specimens, optical microscopy and scanning electron microscope (SEM) were used. From each set of specimens, two specimens were

selected for metallography. The specimens were first ground using sand papers from coarse (i.e. 180 grit size) to fine (i.e. 2000 grit size). The ground surfaces were then polished respectively by 3 μm and 1 μm polishing papers. Two etching solutions were used to reveal the grain boundaries of the polished surfaces from the current study as well as specimens from the previous studies [12, 38] whose S-N curves are adopted in the current study for a more comprehensive analysis. The pure titanium and Ti-6Al-4V specimens were etched using the Kellers etchant (190 ml water + 5 ml nitric acid + 3 ml Hydrochloric acid + 2 ml Hydrofluoric acid) for about 150 s, while another etching solution, i.e. 37%HCl + 1g K2S2O5, was used to etch Co-Cr specimens for 5 min.

The surface morphology, microstructure, and fatigue fracture surfaces were observed with a scanning electron microscope (SEM, JSM-IT100, JEOL). To evaluate the difference between the roughness of Co-Cr and Ti-6Al-4V structures, their roughness values were measured for the same unit cell type (i.e. diamond). Several SEM images were taken from both structure types made from Co-Cr and Ti-6Al-4V structures and the surface roughness was calculated by measuring the diameters at the central part of randomly chosen struts. The surface roughness for both structures were obtained using the arithmetical mean deviation technique:

$$R_a = \frac{1}{n}\sum_{i=1}^{n}|y_i| \tag{1}$$

where $n = 10$ is the number of the struts chosen and y_i is the difference between the diameter of the i^{th} strut and the average diameter.

2.4. Mechanical testing

To have a better understanding of the local mechanical properties of both the bulk and porous structures made of Co-Cr and Ti-6Al-4V structures, Vicker's micro-hardness tests were performed. The polished surfaces of the bulk and porous specimens (with roughness values up to

1 μm) were indented using a Vickers hardness test machine (DuraScan-70, Struers, Netherlands) while applying the HV 0.5 test protocol. The hardness was measured in 20 random positions and the average and standard deviation values were calculated.

The quasi-static mechanical properties of the porous structures were obtained [40] using Instron 5985 in accordance with ISO 13314:2011 [41]. The displacement rate was set to 1.8 mm/min and a 100 kN load cell was used to measure the load. The yield and plateau stresses of the porous structures were used for normalizing their S-N curves. To calculate the yield stress, a line was offset to the right side of the initial linear part of the stress-strain curve for 0.2% and its intersection with the stress-strain curve was obtained. The plateau stress was calculated by obtaining the arithmetical mean of the stress values between 20% and 30% strains [41]. The static mechanical test results for Co-Cr were adopted from our other study [40].

The fatigue tests were performed following the protocols established in our previous studies on the bone-mimicking meta-biomaterials made from Ti-6Al-4V [12, 22], pure titanium [38], and tantalum [39]. All the fatigue tests were compressive-compressive with a minimum to maximum compressive loading ratio of 0.1 and a frequency of 15 Hz. The fatigue tests were stopped after the stiffness of the specimens had reached 10% of their initial value (i.e. when the displacement magnitude was 10 times higher than its initial value). If the specimen did not fail after 10^6 cycles of loading, the test was stopped. For each type of porous structure, the fatigue tests were repeated for several levels of stress and the corresponding fatigue lives were obtained. The stress levels chosen for each porous structure type was chosen in such a way that the meta-biomaterial gave fatigue lives in the range of $10^3 - 10^6$. Using the applied stress level and the resulted fatigue life values, the S-N curve of each specimen was obtained. By dividing the stress in the S-N curve of

each structure by its yield, σ_y, or plateau stress, σ_{pl}, value, the normalized S-N curves of all meta-biomaterials were obtained.

2.5. Statistical analysis

A two-term power series model ($ax^b + c$) was fit to each normalized S-N curve of Co-Cr structures. Lower and upper confidence limits for each fitting was obtained using the Statistics and Machine Learning Toolbox of MATLAB (2013b, MathWorks, USA). The confidence level was chosen as 95%.

3. RESULTS

Microscopic images (Figure 2) demonstrated that the surface of the struts of the meta-biomaterials made from Ti-6Al-4V are coarser than those of the Co-Cr porous structures. Moreover, there was more powder adhered to the struts of Ti-6Al-4V structures as compared to the Co-Cr specimens. The roughness values measured for the Co-Cr porous structure were about half of that of the Ti-6Al-4V porous structure (25.85 μm as compared to 48.46 μm). The percentages of the volume occupied by the internal pores in the struts of Ti-6Al-4V and Co-Cr porous structures were found to be close (97.86±1.49% for Ti-6Al-4V as compared to 98.23±0.55% for Co-Cr). The microstructure was also different in both materials. The Co-Cr microstructure was composed of columnar grains in different directions. Metastable, high-temperature cubic γ phase was observed in the microstructure of Co-Cr specimens, which is likely due to high cooling rates experienced during the SLM process (Figure 3a-b). The Ti-6Al-4V specimens exhibited needle-shaped α′ martensite grains (Figure 3c-d). The α phase normally possesses a lamellar morphology while α' is needle-shaped. Since the SLM process has cooling rates in the order of 106 K/s [42], this results in the transformation of α to α'. The fatigue fracture images showed that there were no uniform crack growth directions in the Co-Cr

specimens and the fracture path was tortuous (Figure 4a). However, the fracture surface of Ti-6Al-4V specimens were relatively flat and the crack propagation was in a uniform direction. Visual examination clearly showed that manufacturing defects like unwelded and unmelted powders are more visible on the strut surface of the Ti-6Al-4V specimens as compared to the Co-Cr specimens (compare Figure 2b with Figure 2d).

The Vickers hardness values for the bulk and porous structures of Co-Cr were close (both around 460), while the Vickers hardness value of Ti-6Al-4V porous structure was 17% lower than that of bulk Ti-6Al-4V material (Table 6). As expected, by increasing the relative density of each type of meta-biomaterials, the absolute compressive stress, $\sigma_{c,max}$, corresponding to the same fatigue life increased (Figure 6). The normalized S-N data points of diamond structure normalized with respect to both yield stress and plateau stress as well as for truncated cuboctahedron structure normalized with respect to plateau stress had small spreads (Figure 7a,b,f). The spread of data points was larger for the other cases (i.e. rhombic dodecahedron structure normalized with respect to both yield stress and plateau stress as well as the truncated cuboctahedron structure normalized with respect to yield stress) (Figure 7c,d,e). The S-N data points of all the structures normalized by yield stress was in the range of 0.48-1.64 (Figure 7, left), while the range for the S-N data points normalized with respect to plateau stress was in the range of 0.31-1.2 (Figure 7, right).

The differences between the normalized S-N curves of meta-biomaterials with the same unit cell type but made of different materials were significant (Figure 8). For all unit cell types, the stress values in the normalized S-N curve of the structures based on Co-Cr were significantly higher than those of the structures made from other materials (Figure 8). Among the meta-biomaterials based on the rhombic dodecahedron unit cell, the highest stress values in the normalized S-N

curve respectively belonged to Co-Cr, pure titanium, tantalum, and Ti-6Al-4V (Figure 8). None of the normalized S-N curves intersected each other in the considered range of cycle numbers (i.e. in the high cycle region). The 95% CIs of the Co-Cr and Ti-6Al-4V structures based on the same unit cell type did not also show any overlapping (Figure 8).

4. DISCUSSIONS

4.1. Topological/material modulation

The results of this study clearly showed that the normalized S-N curves of AM meta-biomaterials are determined by both their topological design and material type (Figure 8-9). Comparing the effects of topological design with those of the material type show that material type influenced the normalized S-N curves to a much greater extent (Figure 9). The S-N curves and 95% confidence limits of meta-biomaterials made from Co-Cr and Ti-6Al-4V constitute two separate clusters, which do not overlap with each other. However, structures made from the same material but based on different unit cells showed considerable overlapping (Figure 9).

The modulated effects of topological design and bulk material properties on the fatigue response of meta-biomaterials is the opposite of what we have found for the *quasi-static* properties of the same meta-biomaterials [40]. In our other study [40], we found that the topological design could result in up to 10-fold difference in the quasi-static mechanical properties of meta-biomaterials, while the effects of material type did not go beyond 2-fold. It would be interesting to extend the current study to other prevalent biocompatible materials as well as other promising unit cell types (see for examples [43]) to see which of the two factors of material type or topological design is more influential in determining the fatigue response of AM meta-biomaterials.

The other interesting difference observed between the fatigue performance of meta-biomaterials made of Co-Cr and that of Ti-6Al-4V was the maximum strength recorded in their S-N curves

normalized with respect to yield stress (Figure 7 left and Figure 8, see also [12]). The maximum fatigue strength of meta-biomaterials made of Ti-6Al-4V did not exceed 80-90% of the yield stress (in cycles around $10^3 - 10^4$) [12, 22]. By setting the applied stress in the fatigue test of meta-biomaterials made of Ti-6Al-4V to values around 90% of yield stress, the structure experienced immediate fatigue failure before reaching 100 cycles. The maximum fatigue strength of meta-biomaterials made of Co-Cr, however, could go up to values around 170% of their yield strengths (in cycles around $10^3 - 10^4$) (Figure 7 left). A similar trend has been observed in the literature regarding the high fatigue strength of Co-Cr *solid* materials which showed fatigue strengths around 130% of yield stress [44], 99% of yield stress [45], and 127% of yield stress [46] at 10^5 cycles. In the same studies, fatigue strengths around 124% of yield stress [45] and 150% of yield stress [46] at cycle numbers around 10^4 was reported. This is another observation that signifies the importance of material type in determining the fatigue response of meta-biomaterials.

Ideally, one would like to use scaffolds that have exactly same morphological parameters. In this study, however, we also used the data available from several studies that were previously performed and whose designs changed during the current study. There were therefore some differences in the absolute values of morphological parameters between the different material types. In particular, the strut size of the Co-Cr porous structures used in this study was almost twice that of the reported Ti-6Al-4V and Ta scaffolds. This may have also contributed to the improved fatigue behavior of Co-Cr-Mo scaffolds as compared to other materials.

4.2. The effects of surface roughness and grain morphology

Surface roughness affects the fatigue crack initiation because stress concentration is drastically raised in sharp-angled particles. One of the reasons behind the higher fatigue lives of Co-Cr

structures as compared to Ti-6Al-4V specimens could be the much smoother surface of the Co-Cr porous structures (Figure 2). Moreover, the columnar grains of Co-Cr grow in different orientations and could therefore interlock each other [47]. The texture resembling a common weaved fabric could improve the fatigue resistance of the material, as the crack path will be more tortuous then and the fatigue crack growth rate will likely slow down. Figure 4(a) shows the crack propagation tortured in different orientations. The crack propagation energy could be absorbed at multiple scales, respectively, by the microscopically weaved elongated grains and by the grain boundaries, resulting in longer fatigue lives of Co-Cr structures.

As for the SLM Ti-6Al-4V, the microstructure is of needle α′ martensite type due to the rapid cooling rate. As is clear from Figure 4(b), the cracks grew along the needle-shaped grains. The crack growth resistance seems to be lower and the crack surface is fairly smooth. The low ductility of the martensite phase in Ti-6Al-4V implies sensitivity to notches. This could be another explanation for the shorter fatigue lives observed. We also found more manufacturing defects in Ti-6Al-4V struts. The internal pores and unmelted powders on the surface could both serve as stress concentration sites for fatigue crack initiation. Although the internal pore volume percentage was similar and negligible in both the materials, the much higher external surface roughness in the Ti-6Al-4V structures (Figure 2) could lead to more significant decrease in the fatigue life of Ti-6Al-4V meta-biomaterials as compared to Co-Cr structures. The hardness tests also demonstrated the detrimental effects of rapid cooling on porous Ti-6Al-4V specimens (i.e. 17% reduction in the local hardness as compared to bulk Ti-6Al-4V), while the rapid cooling effect was almost negligible in Co-Cr porous structures (Table 6).

In surface-finished parts, the design geometry of the part plays an important role in determining the stress concentration factor. In AM porous structures with pore sizes smaller than 1 mm,

however, the irregularities created by the manufacturing processes play the dominant role in determining the stress concentration factor. These irregularities in the external surface are created by first large melt pools the size of which is comparable to the strut size and second by unmelted powders on the surface. While the stress concentration effect of the powder particles adhered to the final product is similar in the porous structures with different relative density, the effect of melt pool size on the stress concentration factor becomes larger as the nominal strut diameter decreases. This is due to the fact that as the nominal strut diameter decreases the ratio of the melt pool size to the nominal strut diameter increases (compare Figure 10a and 10b). This can also explain the lower lives of structures with lower relative densities. Moreover, the stress concentration factors are expected to be higher for scaffolds with higher roughness values. For example, the stress concentration factors of Ti-6Al-4V specimens are expected to be higher than those of Co-Cr specimens

4.3. The effects of the mechanical behavior of the bulk material

Our results demonstrated that the normalized fatigue strengths of meta-biomaterials made of Co-Cr are much higher than those of other meta-biomaterials (Figure 8-9). This could be attributed to the intrinsic properties of stress concentration factor and its different effects on fatigue and static loadings as well as to the difference in the mechanical behavior of the bulk material. Co-Cr specimens demonstrate higher levels of strain-hardening while the degree of strain hardening in pure titanium and Ti-6Al-4V is much less. In other words, the difference between ultimate stress and yield stress in bulk Co-Cr is significant (our tests [40] demonstrated that ultimate stress is about 3-4 times larger than the yield stress) while in pure titanium and Ti-6Al-4V they are relatively close. In Co-Cr porous structures, due to high strain-hardening capacity, the effects of stress concentration are offset by local plasticity particularly in the vicinity of crack front. In Ti-

6Al-4V structures, due to much less strain-hardening capacity, the stress-concentration effects lead to quicker crack initiation and therefore quicker failure in the struts of the porous structures. This could explain why the normalized S-N curves of Ti-6Al-4V meta-biomaterials are generally much lower than those of Co-Cr meta-biomaterials.

The results also demonstrated that in the normalized S-N curves of porous structures, the spread of the data points is greater in Co-Cr specimens as compared to Ti-6Al-4V, pure titanium, and tantalum specimens. In particular, the spread of the data points was relatively large in Co-Cr rhombic dodecahedron and truncated cuboctahedron cases. In the normalized S-N curves of Co-Cr meta-biomaterials based on the same unit cell type, as the relative density of the porous structure increased, the data points of the meta-biomaterials with higher relative densities lie higher. This could be once more attributed to the post-elastic behavior of the bulk Co-Cr material. It has been reported [40] that by increasing the relative density, the porous Co-Cr material shows more strain-hardening behavior in its stress-strain curve before reaching the first maximum stress. This is expected, as the similarity between the fatigue response of porous structures and that of the bulk Co-Cr material should increase with relative density. It is worth noting that bulk Co-Cr exhibits S-N data points that are as large as 150% of its yield stress [44-46]). That is why the normalized S-N curves of structures with higher relative densities tend to be higher than those with lower relative densities, and therefore a spread in normalized S-N curve is observed.

4.4. HCF/LCF differences

The fatigue response of meta-biomaterials depends not only on the static and fatigue behavior of the bulk material and topological design but also on the roughness of the outer surface of the struts (which greatly affects crack initiation), distribution of the micro-pores created inside the

struts during the AM process (which affects the crack propagation mechanism), and plasticity (which affects both crack initiation and crack propagation mechanisms). Effects such as surface finish and material imperfections are more dominant in high cycle fatigue (HCF) range as compared to low cycle fatigue (LCF), because their influence increases as the stress level decreases. This is due to the fact that in HCF, the crack nucleation occurs due to intrusion and extrusion in the material. However, in LCF, the main cause of crack nucleation is bulk plastic deformations. The effects of surface irregularities and the material internal imperfections are therefore much less apparent in LCF as compared to HCF. As is clear from Figure 9, the material and imperfection effects are most prominent in the HCF region. For example, for the rhombic dodecahedron unit cell, for fatigue lives around 10^4 cycles (i.e. LCF), the ratio of the stress level of Co-Cr porous structure to that of the Ti-6Al-4V porous structure is about 2.58:1. For fatigue lives around 10^6 cycles (i.e. HCF), the noted ratio becomes about 5.5:1. As another example, for the diamond unit cell type, for fatigue lives around 10^4 cycles (i.e. LCF), the ratio of the stress level of Co-Cr porous structure to that of the Ti-6Al-4V porous structure is about 1.68:1, while for fatigue lives around 10^6 cycles (i.e. HCF) the noted ratio is about 2.6:1. Empirical approaches are typically used to account for imperfection effects particularly when using the S-N approach. Another type of effect comes from cyclic plasticity, which typically is more prominent in the LCF as compared to HCF. Those include effects such as strain hardening, cyclic softening or hardening, stress gradient, etc. Such effects are more prominent in the LCF due to the higher plastic deformation in this regime. It is difficult to account for those effects using empirical approaches and, therefore, more analytical methods such as strain-life method are more suited. As it can be seen in Figure 9, the S-N curves of the Co-Cr and Ti-6Al-4V structures become closer to each other in the LCF. It is not easy to say which of the two parameters of

manufacturing imperfection and post-elastic material behavior of Co-Cr or Ti-6Al-4V stand for this significant decrease in the difference between the S-N curves of the two structures in LCF as compared to HCF in Figure 9. Due to intrinsic differences in the AM parameters such as powder size, laser power, layer thickness, and working temperature used to manufacture meta-biomaterials made of different materials, it is difficult to answer the above-mentioned question using only empirical methods. To better distinguish between the material and manufacturing imperfection effects, computational methods [48] could be implemented to investigate the effects of each parameter exclusively by keeping other parameters unchanged. Using computational methods such as the finite element method, it is also possible to study the changes in the local stresses and strains in the most vulnerable locations of each unit cell type, which itself can be obtained using microscopic imaging as well as finite element modeling. Effects such as multiaxial stresses could also become important in AM meta-biomaterials due to the complex loading conditions in the struts and vertices of the porous structures.

In the LCF regime, it might be better to use methods not just based on stress or strain, but both. For example, when material response changes based on the applied stress, such as in strain hardening or cyclic hardening/softening, such approaches (for example SWT [49, 50], Fatemi-Socie [51], energy methods [52, 53], etc.) are more quantitative and could better account for those effects. It should be kept in mind that discussing the fatigue response in terms of LCF and HCF is only useful for distinguishing the main trends, as such a classification typically only applies to constant applied loading. The realistic loading conditions of most components and structures, including biomedical implants is variable amplitude. In such loading cases, there are many low amplitude cycles belonging to HCF and some overload cycles belonging to LCF.

Therefore, such problems cannot be classified as either LCF or HCF. The approaches incorporating both stress and strain typically work better for this class of problems.

4.5. Loading condition

Although after implantation, the porous structures are usually loaded in both compression and bending loads, in this study, similar to previous studies in the literature [12, 18-22], only the compression-compression tests were carried out for comparing the performance of porous structures with different topological designs and made from different materials. Testing the fatigue behavior of meta-biomaterials under bending load is more challenging, as the loading conditions will be dependent on the anatomical site, the type of implant, and anatomical features of the patient. In comparison, the number of factors in axial compression-compression testing is more limited. However, to validate an implant (with or without porous body), it is always recommended to carry out experimental fatigue tests with loading conditions which are chosen to be as close as possible to the actual loading conditions experienced in the human body.

4.6. Applications in biomedical implants

As previously mentioned, AM meta-biomaterials need to satisfy several requirements regarding their mechanical, mass transport (e.g. permeability, diffusivity), and topological (e.g. curvature) properties in order to qualify as suitable bone substitutes. It is often assumed that the various properties of AM meta-biomaterials should mimic those of the native bone tissue. Since there are significant variations in the properties of the native bone tissue, it is generally more appropriate to present a range of acceptable properties. All AM porous meta-biomaterials considered here show elastic moduli in the range of those reported for bone [40, 54-56]. As for the fatigue behavior, the S-N curves determined here and in the previous studies are often used to determine the stress level for which the implants could undergo at least one million of loading cycles

without failure. Regarding the bio-compatibility requirements, all included materials are considered to be sufficiently bio-compatible [57, 58]. In certain applications of AM meta-biomaterials including treatment of critical sized bony defects, it is often ideal to use biodegradable metallic biomaterials that break down after fully regenerating functional bone tissue. None of the materials considered here are biodegradable. Indeed, the progress in development of AM biodegradable metallic meta-biomaterials has been very limited so far. Ultimately, all the developed meta-biomaterials need to be tested in animal models and clinical studies before routine clinical application. Our previous animal studies have shown the potential of both AM porous Ti-6Al-4V [59, 60] and AM porous tantalum [39] for treatment of critical size bony defects. The *in vivo* response to Co-Cr alloys may not be as favorable as the response to titanium alloys [61]. However, it has been recently shown that adding small amounts of Zr could significantly improve the osseointegration of Co-Cr implants [62].

5. CONCLUSIONS

We studied the isolated and modulated effects of topological design and material type on the fatigue behavior of AM meta-biomaterials. The relative density of the Co-Cr meta-biomaterials based on diamond unit cell did not have a significant effect on their normalized S-N curves similar to what was previously observed for Ti-6Al-4V structures based on all the unit cell types. However, unlike what had been previously observed for Ti-6Al-4V structures, the relative density had a considerable effect on the normalized S-N curves of Co-Cr porous structures based on truncated cuboctahedron and particularly rhombic dodecahedron unit cells. These differences could be attributed to the large difference between the post-elastic behavior of Co-Cr as compared to the other considered materials. Bulk Co-Cr material showed a substantial strain-hardening behavior which also leads to its very high fatigue strength (previous studies have

shown that it can have S-N data points as large as 150% of its yield stress [44-46]). As the relative density increases, the fatigue response of porous structure becomes more similar to the bulk Co-Cr material and topology contributes less to the fatigue response. It was observed that, in general, as compared to the topological design (unit cell type and porosity), the material type and manufacturing imperfections are more important in determining the normalized S-N curves of AM meta-biomaterials particularly in the HCF region. This is the opposite of what we found for the quasi-static mechanical properties of the same materials and topologies. The effects of material type, manufacturing imperfections, and topological design were different in the LCF and HCF regions. That is due to the fact that the fatigue response of AM meta-biomaterials is dependent not only on the static and fatigue strengths of the bulk material but also on other factors such as the roughness of the outer surface of the struts (affecting crack initiation), distribution of the micro-pores created inside the struts during the AM process (affecting crack propagation procedure), and plasticity (affecting both crack initiation and crack propagation procedures). The contribution of each of the noted parameters is different in the HCF and LCF regions.

REFERENCES

1. Valentine, J., S. Zhang, T. Zentgraf, E. Ulin-Avila, D.A. Genov, G. Bartal, and X. Zhang, *Three-dimensional optical metamaterial with a negative refractive index.* nature, 2008. **455**(7211): p. 376-379.
2. Zhao, Y., M. Belkin, and A. Alù, *Twisted optical metamaterials for planarized ultrathin broadband circular polarizers.* Nature communications, 2012. **3**: p. 870.
3. Menzel, C., C. Helgert, C. Rockstuhl, E.-B. Kley, A. Tünnermann, T. Pertsch, and F. Lederer, *Asymmetric transmission of linearly polarized light at optical metamaterials.* Physical review letters, 2010. **104**(25): p. 253902.
4. Shalaev, V.M., W. Cai, U.K. Chettiar, H.-K. Yuan, A.K. Sarychev, V.P. Drachev, and A.V. Kildishev, *Negative index of refraction in optical metamaterials.* Optics letters, 2005. **30**(24): p. 3356-3358.
5. Lee, J.H., J.P. Singer, and E.L. Thomas, *Micro-/Nanostructured Mechanical Metamaterials.* Advanced materials, 2012. **24**(36): p. 4782-4810.
6. Akagawa, Y., Y. Ichikawa, H. Nikai, and H. Tsuru, *Interface histology of unloaded and early loaded partially stabilized zirconia endosseous implant in initial bone healing.* The Journal of prosthetic dentistry, 1993. **69**(6): p. 599-604.

7. Hedayati, R., A. Leeflang, and A. Zadpoor, *Additively manufactured metallic pentamode meta-materials.* Applied Physics Letters, 2017. **110**(9): p. 091905.
8. Zadpoor, A.A., *Mechanical meta-materials.* Materials Horizons, 2016. **3**(5): p. 371-381.
9. Torrent, D. and J. Sánchez-Dehesa, *Acoustic metamaterials for new two-dimensional sonic devices.* New journal of physics, 2007. **9**(9): p. 323.
10. Chen, H. and C. Chan, *Acoustic cloaking in three dimensions using acoustic metamaterials.* Applied physics letters, 2007. **91**(18): p. 183518.
11. Zhang, S., L. Yin, and N. Fang, *Focusing ultrasound with an acoustic metamaterial network.* Physical review letters, 2009. **102**(19): p. 194301.
12. Amin Yavari, S., S. Ahmadi, R. Wauthle, B. Pouran, J. Schrooten, H. Weinans, and A. Zadpoor, *Relationship between unit cell type and porosity and the fatigue behavior of selective laser melted meta-biomaterials.* Journal of the mechanical behavior of biomedical materials, 2015. **43**: p. 91-100.
13. Fielding, G.A., A. Bandyopadhyay, and S. Bose, *Effects of silica and zinc oxide doping on mechanical and biological properties of 3D printed tricalcium phosphate tissue engineering scaffolds.* Dental Materials, 2012. **28**(2): p. 113-122.
14. Wu, C., Y. Ramaswamy, P. Boughton, and H. Zreiqat, *Improvement of mechanical and biological properties of porous CaSiO 3 scaffolds by poly (d, l-lactic acid) modification.* Acta Biomaterialia, 2008. **4**(2): p. 343-353.
15. Hollister, S.J., *Porous scaffold design for tissue engineering.* Nature materials, 2005. **4**(7): p. 518-524.
16. Drury, J.L. and D.J. Mooney, *Hydrogels for tissue engineering: scaffold design variables and applications.* Biomaterials, 2003. **24**(24): p. 4337-4351.
17. Meinel, L., V. Karageorgiou, R. Fajardo, B. Snyder, V. Shinde-Patil, L. Zichner, D. Kaplan, R. Langer, and G. Vunjak-Novakovic, *Bone tissue engineering using human mesenchymal stem cells: effects of scaffold material and medium flow.* Annals of biomedical engineering, 2004. **32**(1): p. 112-122.
18. Hrabe, N.W., P. Heinl, B. Flinn, C. Körner, and R.K. Bordia, *Compression-compression fatigue of selective electron beam melted cellular titanium (Ti-6Al-4V).* Journal of Biomedical Materials Research Part B: Applied Biomaterials, 2011. **99**(2): p. 313-320.
19. Zhao, S., S. Li, W. Hou, Y. Hao, R. Yang, and R. Misra, *The influence of cell morphology on the compressive fatigue behavior of Ti-6Al-4V meshes fabricated by electron beam melting.* Journal of the mechanical behavior of biomedical materials, 2016. **59**: p. 251-264.
20. Yan, C., L. Hao, A. Hussein, and P. Young, *Ti–6Al–4V triply periodic minimal surface structures for bone implants fabricated via selective laser melting.* journal of the mechanical behavior of biomedical materials, 2015. **51**: p. 61-73.
21. Yavari, S.A., S. Ahmadi, R. Wauthle, B. Pouran, J. Schrooten, H. Weinans, and A. Zadpoor, *Relationship between unit cell type and porosity and the fatigue behavior of selective laser melted meta-biomaterials.* Journal of the mechanical behavior of biomedical materials, 2015. **43**: p. 91-100.
22. Yavari, S.A., R. Wauthlé, J. van der Stok, A. Riemslag, M. Janssen, M. Mulier, J.-P. Kruth, J. Schrooten, H. Weinans, and A.A. Zadpoor, *Fatigue behavior of porous biomaterials manufactured using selective laser melting.* Materials Science and Engineering: C, 2013. **33**(8): p. 4849-4858.
23. Babaee, S., B.H. Jahromi, A. Ajdari, H. Nayeb-Hashemi, and A. Vaziri, *Mechanical properties of open-cell rhombic dodecahedron cellular structures.* Acta Materialia, 2012. **60**(6): p. 2873-2885.
24. Ahmadi, S., S. Yavari, R. Wauthle, B. Pouran, J. Schrooten, H. Weinans, and A. Zadpoor, *Additively manufactured open-cell porous biomaterials made from six different space-filling unit cells: the mechanical and morphological properties.* Materials, 2015. **8**(4): p. 1871-1896.

25. Hedayati, R., M. Sadighi, M. Mohammadi-Aghdam, and A. Zadpoor, *Analytical relationships for the mechanical properties of additively manufactured porous biomaterials based on octahedral unit cells.* Applied Mathematical Modelling, 2017. **46**: p. 408-422.
26. Zheng, X., H. Lee, T.H. Weisgraber, M. Shusteff, J. DeOtte, E.B. Duoss, J.D. Kuntz, M.M. Biener, Q. Ge, and J.A. Jackson, *Ultralight, ultrastiff mechanical metamaterials.* Science, 2014. **344**(6190): p. 1373-1377.
27. Hedayati, R., M. Sadighi, M. Mohammadi Aghdam, and A.A. Zadpoor, *Mechanical properties of additively manufactured thick honeycombs.* Materials, 2016. **9**(8): p. 613.
28. Balla, V.K., S. Bodhak, S. Bose, and A. Bandyopadhyay, *Porous tantalum structures for bone implants: fabrication, mechanical and in vitro biological properties.* Acta biomaterialia, 2010. **6**(8): p. 3349-3359.
29. Yan, C., L. Hao, A. Hussein, P. Young, and D. Raymont, *Advanced lightweight 316L stainless steel cellular lattice structures fabricated via selective laser melting.* Materials & Design, 2014. **55**: p. 533-541.
30. Tsopanos, S., R. Mines, S. McKown, Y. Shen, W. Cantwell, W. Brooks, and C. Sutcliffe, *The influence of processing parameters on the mechanical properties of selectively laser melted stainless steel microlattice structures.* Journal of Manufacturing Science and Engineering, 2010. **132**(4): p. 041011.
31. Kirkland, N., I. Kolbeinsson, T. Woodfield, G. Dias, and M. Staiger, *Synthesis and properties of topologically ordered porous magnesium.* Materials Science and Engineering: B, 2011. **176**(20): p. 1666-1672.
32. Nguyen, T.L., M.P. Staiger, G.J. Dias, and T.B. Woodfield, *A Novel Manufacturing Route for Fabrication of Topologically-Ordered Porous Magnesium Scaffolds.* Advanced Engineering Materials, 2011. **13**(9): p. 872-881.
33. Sun, J., Y. Yang, and D. Wang, *Mechanical properties of a Ti6Al4V porous structure produced by selective laser melting.* Materials & Design, 2013. **49**: p. 545-552.
34. Lipinski, P., A. Barbas, and A.-S. Bonnet, *Fatigue behavior of thin-walled grade 2 titanium samples processed by selective laser melting. Application to life prediction of porous titanium implants.* journal of the mechanical behavior of biomedical materials, 2013. **28**: p. 274-290.
35. Parthasarathy, J., B. Starly, S. Raman, and A. Christensen, *Mechanical evaluation of porous titanium (Ti6Al4V) structures with electron beam melting (EBM).* Journal of the mechanical behavior of biomedical materials, 2010. **3**(3): p. 249-259.
36. Han, C., X. Chen, J. Tan, Y. Yao, Q. Wei, Z. Zhang, and Y. Shi, *Surface modification on a porous Co-Cr scaffold fabricated by selective laser melting for bone implant applications.*
37. Han, C., C. Han, C. Yan, C. Yan, S. Wen, S. Wen, T. Xu, T. Xu, S. Li, and S. Li, *Effects of the unit cell topology on the compression properties of porous Co-Cr scaffolds fabricated via selective laser melting.* Rapid Prototyping Journal, 2017. **23**(1): p. 16-27.
38. Wauthle, R., S.M. Ahmadi, S.A. Yavari, M. Mulier, A.A. Zadpoor, H. Weinans, J. Van Humbeeck, J.-P. Kruth, and J. Schrooten, *Revival of pure titanium for dynamically loaded porous implants using additive manufacturing.* Materials Science and Engineering: C, 2015. **54**: p. 94-100.
39. Wauthle, R., J. Van der Stok, S.A. Yavari, J. Van Humbeeck, J.-P. Kruth, A.A. Zadpoor, H. Weinans, M. Mulier, and J. Schrooten, *Additively manufactured porous tantalum implants.* Acta biomaterialia, 2015. **14**: p. 217-225.
40. Hedayati, R., S.M. Ahmadi, K. Lietaert, B. Pouran, Y. Li, H. Weinans, C.D. Rans, and A.A. Zadpoor, *Isolated and modulated effects of topology and material type on the mechanical properties of additively manufactured porous biomaterials.* Submitted.
41. Standard, I., *ISO 13314: 2011 (E)(2011) Mechanical testing of metals—ductility testing—compression test for porous and cellular metals.* Ref Number ISO. **13314**(13314): p. 1-7.
42. Zheng, Y., X. Xu, Z. Xu, H. Cai, and J.-Q. Wang, *Metallic Biomaterials: New Directions and Technologies*. 2017: John Wiley & Sons.

43. Zadpoor, A.A. and R. Hedayati, *Analytical relationships for prediction of the mechanical properties of additively manufactured porous biomaterials.* Journal of Biomedical Materials Research Part A, 2016. **104**(12): p. 3164–3174.
44. *ASTM F75 CoCr Alloy*, A.E. system, Editor.: Mölndal, Sweden.
45. Marrey, R.V., R. Burgermeister, R.B. Grishaber, and R. Ritchie, *Fatigue and life prediction for cobalt-chromium stents: A fracture mechanics analysis.* Biomaterials, 2006. **27**(9): p. 1988-2000.
46. Okazaki, Y., *Comparison of fatigue properties and fatigue crack growth rates of various implantable metals.* Materials, 2012. **5**(12): p. 2981-3005.
47. Qian, B., K. Saeidi, L. Kvetková, F. Lofaj, C. Xiao, and Z. Shen, *Defects-tolerant Co-Cr-Mo dental alloys prepared by selective laser melting.* Dental Materials, 2015. **31**(12): p. 1435-1444.
48. Hedayati, R., M. Sadighi, M. Mohammadi-Aghdam, and A.A. Zadpoor, *Computational prediction of the fatigue behavior of additively manufactured porous metallic biomaterials* International journal of fatigue, 2016. **84**: p. 67–79.
49. Stephens, R., P. Dindinger, and J. Gunger, *Fatigue damage editing for accelerated durability testing using strain range and SWT parameter criteria.* International Journal of fatigue, 1997. **19**(8): p. 599-606.
50. Wu, Z.-R., X.-T. Hu, and Y.-D. Song, *Multiaxial fatigue life prediction for titanium alloy TC4 under proportional and nonproportional loading.* International Journal of Fatigue, 2014. **59**: p. 170-175.
51. Fatemi, A. and D.F. Socie, *A Critical Plane Approach to Multiaxial Fatigue Damage Including out-of-Phase Loading.* Fatigue & Fracture of Engineering Materials & Structures, 1988. **11**(3): p. 149-165.
52. Morrow, J., *Cyclic plastic strain energy and fatigue of metals*, in *Internal friction, damping, and cyclic plasticity*. 1965, ASTM International.
53. Moumni, Z., A. Van Herpen, and P. Riberty, *Fatigue analysis of shape memory alloys: energy approach.* Smart Materials and Structures, 2005. **14**(5): p. S287.
54. Zysset, P.K., X.E. Guo, C.E. Hoffler, K.E. Moore, and S.A. Goldstein, *Elastic modulus and hardness of cortical and trabecular bone lamellae measured by nanoindentation in the human femur.* Journal of biomechanics, 1999. **32**(10): p. 1005-1012.
55. Bayraktar, H.H., E.F. Morgan, G.L. Niebur, G.E. Morris, E.K. Wong, and T.M. Keaveny, *Comparison of the elastic and yield properties of human femoral trabecular and cortical bone tissue.* Journal of biomechanics, 2004. **37**(1): p. 27-35.
56. Rho, J.-Y., L. Kuhn-Spearing, and P. Zioupos, *Mechanical properties and the hierarchical structure of bone.* Medical engineering & physics, 1998. **20**(2): p. 92-102.
57. Krishna, B.V., W. Xue, S. Bose, and A. Bandyopadhyay, *Functionally graded Co–Cr–Mo coating on Ti–6Al–4V alloy structures.* Acta biomaterialia, 2008. **4**(3): p. 697-706.
58. Matsuno, H., A. Yokoyama, F. Watari, M. Uo, and T. Kawasaki, *Biocompatibility and osteogenesis of refractory metal implants, titanium, hafnium, niobium, tantalum and rhenium.* Biomaterials, 2001. **22**(11): p. 1253-1262.
59. Van Der Stok, J., D. Lozano, Y.C. Chai, S. Amin Yavari, A.P. Bastidas Coral, J.A. Verhaar, E. Gómez-Barrena, J. Schrooten, H. Jahr, and A.A. Zadpoor, *Osteostatin-coated porous titanium can improve early bone regeneration of cortical bone defects in rats.* Tissue Engineering Part A, 2015. **21**(9-10): p. 1495-1506.
60. Van der Stok, J., O.P. Van der Jagt, S. Amin Yavari, M.F. De Haas, J.H. Waarsing, H. Jahr, E.M. Van Lieshout, P. Patka, J.A. Verhaar, and A.A. Zadpoor, *Selective laser melting-produced porous titanium scaffolds regenerate bone in critical size cortical bone defects.* Journal of Orthopaedic Research, 2013. **31**(5): p. 792-799.
61. Jakobsen, S.S., J. Baas, T. Jakobsen, and K. Soballe, *Biomechanical implant fixation of CoCrMo coating inferior to titanium coating in a canine implant model.* Journal of Biomedical Materials Research Part A, 2010. **94**(1): p. 180-186.

62. Stenlund, P., S. Kurosu, Y. Koizumi, F. Suska, H. Matsumoto, A. Chiba, and A. Palmquist, *Osseointegration enhancement by Zr doping of Co-Cr-Mo implants fabricated by electron beam melting.* Additive Manufacturing, 2015. **6**: p. 6-15.
63. Ahmadi, S., G. Campoli, S. Amin Yavari, B. Sajadi, R. Wauthlé, J. Schrooten, H. Weinans, and A.A. Zadpoor, *Mechanical behavior of regular open-cell porous biomaterials made of diamond lattice unit cells.* Journal of the mechanical behavior of biomedical materials, 2014. **34**: p. 106-115.

List of figure captions

Tables

Table 1- Topological design and morphological properties of the porous structures made from Co-Cr alloy [40]

Co-Cr (L=20 mm, D=15 mm)						
	Relative density		Strut size (μm)		Pore size (μm)	
	Dry weighting	μCT	Nominal (Design)	μCT	Nominal (Design)	μCT
Truncated cuboctahedron (TCO)						
TCO-1	0.236	0.27	324	343.2	876	917.76
TCO-2	0.269	0.28	356	339.84	844	895.2
TCO-3	0.336	0.334	410	396.96	790	821.472
TCO-4	0.386	0.424	460	433.584	740	669.312
Rhombic dodecahedron (RD)						
RD-1	0.299	0.292	310	349.44	590	506.256
RD-2	0.372	0.475	370	402.528	530	492.576
RD-3	0.415	0.532	430	446.4	470	431.76
Diamond (D)						
D-1	0.209	0.272	320	357.216	580	650.736
D-2	0.267	0.35	375	390.384	525	541.488
D-3	0.34	0.445	415	440.928	485	465.6
D-4	0.401	0.526	450	486.288	450	411.36

Table 2- Topological design and morphological properties of the porous structures made from Ti-6Al-4V alloy [12, 22]

Ti-6Al-4V (L=15 mm, D=10 mm)						
	Relative density		Strut size (μm)		Pore size (μm)	
	Dry weighting	μCT	Nominal (Design)	μCT	Nominal (Design)	μCT
Truncated cuboctahedron (TCO)						
TCO-1	0.2	0.17	234	350	876	862
TCO-2	0.22	0.2	460	416	1040	1142
TCO-3	0.27	0.27	577	482	923	1079
TCO-4	0.33	0.36	693	564	807	1049
Rhombic dodecahedron (RD)						
RD-1	0.163	0.158	120	140	500	560
RD-2	0.229	0.223	170	218	500	608
RD-3	0.299	0.288	170	216	450	486
RD-4	0.336	0.342	230	251	500	560
Diamond (D)						
D-1	0.11	0.11	277	240	923	958
D-2	0.2	0.21	450	363	750	780
D-3	0.26	0.28	520	472	680	719
D-4	0.34	0.36	600	536	600	641

Table 3- Topological design and morphological properties of the porous structures made from pure titanium [38]

Pure titanium (L=15 mm, D=10 mm)						
	Relative density		Strut size (μm)		Pore size (μm)	
	Dry weighting	Archimedes	Nominal (Design)	μCT	Nominal (Design)	μCT
Rhombic dodecahedron (RD)						
RD-1	0.183	0.184	120	-	500	-
RD-2	0.215	0.216	170		500	
RD-3	0.286	0.289	170		450	
RD-4	0.333	0.34	230		500	

Table 4- Topological design and morphological properties of the porous structures made from tantalum [39]

Tantalum (L=15 mm, D=10 mm)						
	Relative density		Strut size (μm)		Pore size (μm)	
	Dry weighting	Archimedes	Nominal (Design)	μCT	Nominal (Design)	μCT
Rhombic dodecahedron (RD)						
RD	0.201	0.203	150	-	500	-

Table 5- Mechanical properties of the bulk materials [40]

	$\sigma_{y,s}$ [MPa]	E_s [GPa]
Ti-6Al-4V [63]	980	122
Co-Cr [40]	657	201.5 (Mechanical test) 205 (Impulse Excitation)
Commercial pure titanium [38]	300	100
Tantalum [39]	180	179

Table 6- Vickers hardness values obtained from the hardness tests

	Bulk	**Porous**
Co-Cr	460 ± 28.897	460.75 ± 29.994
Ti-6Al-4V	523.25 ± 47.4983	433.142 ± 8.952

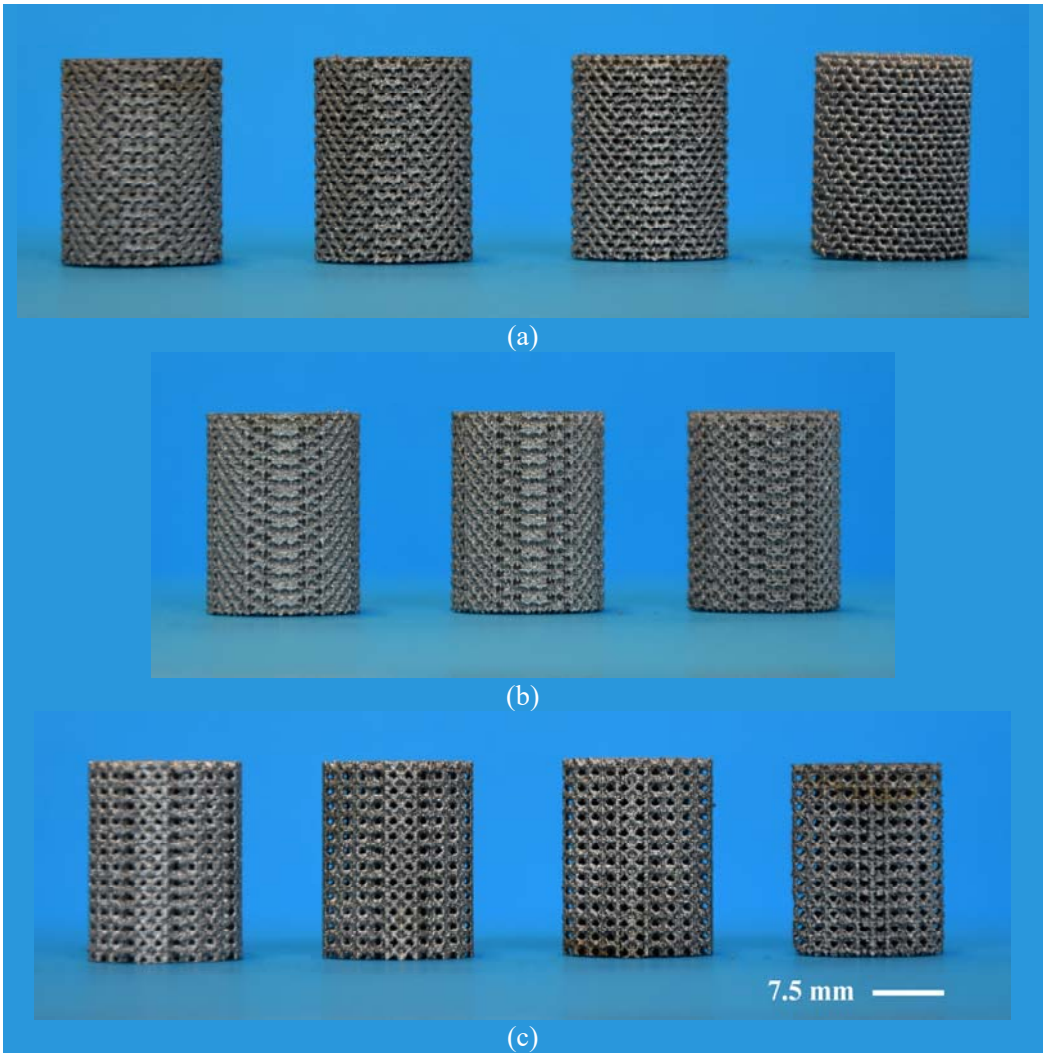

Figure 1- Side view of the additively manufactured Co-Cr porous structures based on (a) diamond (b) rhombic dodecahedron, and (c) truncated cuboctahedron unit cells [40]

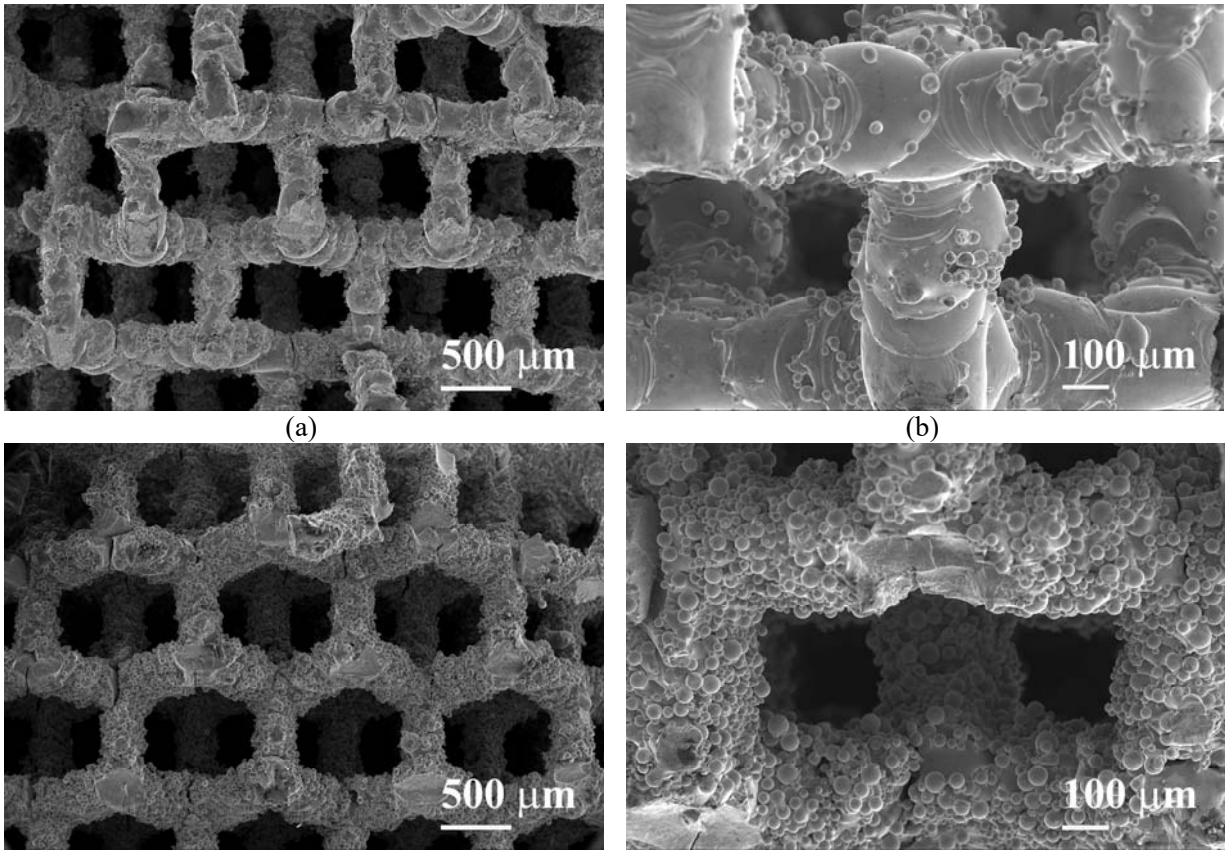

(a) (b)

(c) (d)

Figure 2- Strut surface morphology of selective laser melted (a) Co-Cr (magnification: X30), (b) Co-Cr (magnification: X100), (c) Ti-6Al-4V (magnification: X30), and (d) Ti-6Al-4V (magnification: X100) porous structures based on diamond unit cell

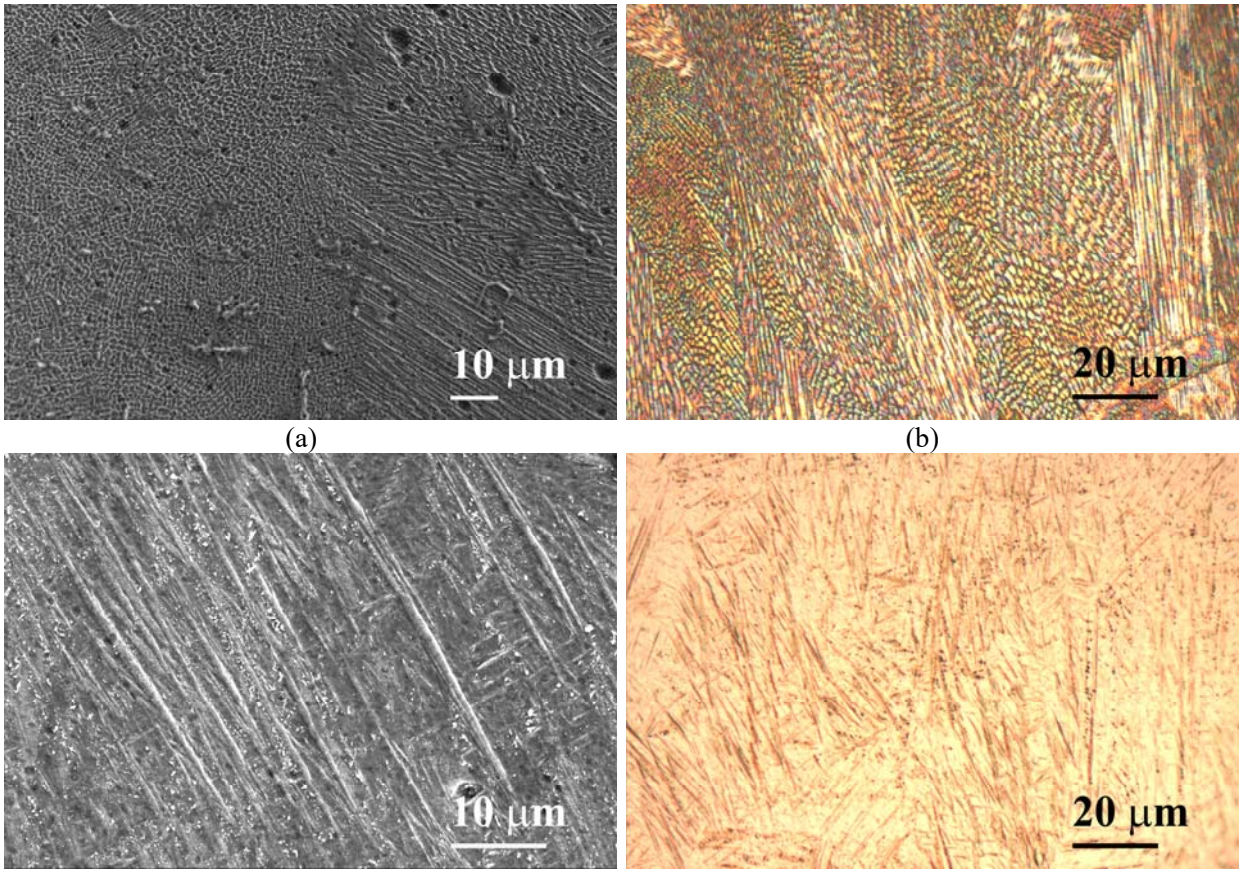

(a) (b)

(c) (d)

Figure 3- SEM and optical microscopy images of the microstructure of the struts in selective laser melted (a-b) Co-Cr and (c-d) Ti-6Al-4V porous structure.

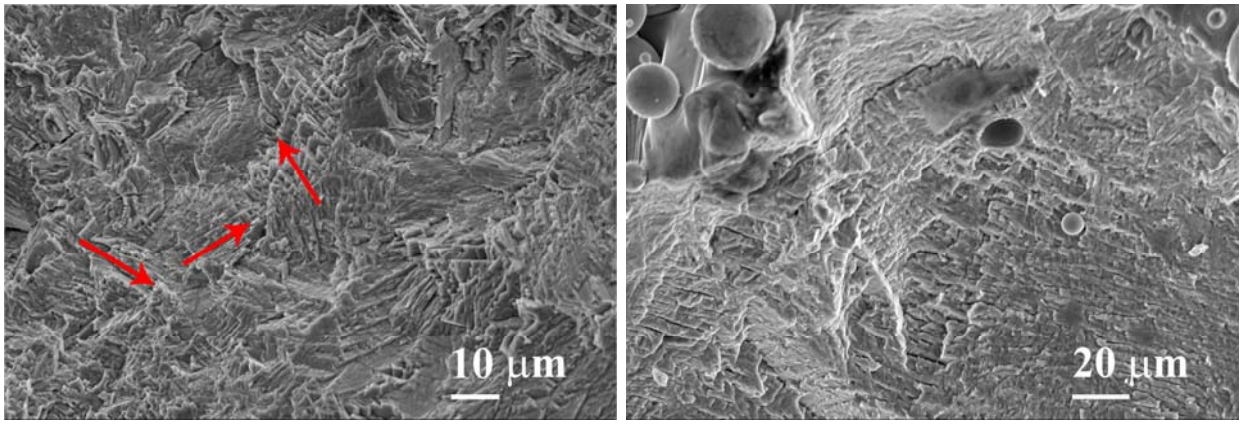

(a) (b)

Figure 4- Fatigue fracture morphology of the struts in selective laser melted (a) Co-Cr and (b) Ti-6Al-4V porous structure. Fatigue fracture surfaces are indicated by red arrows.

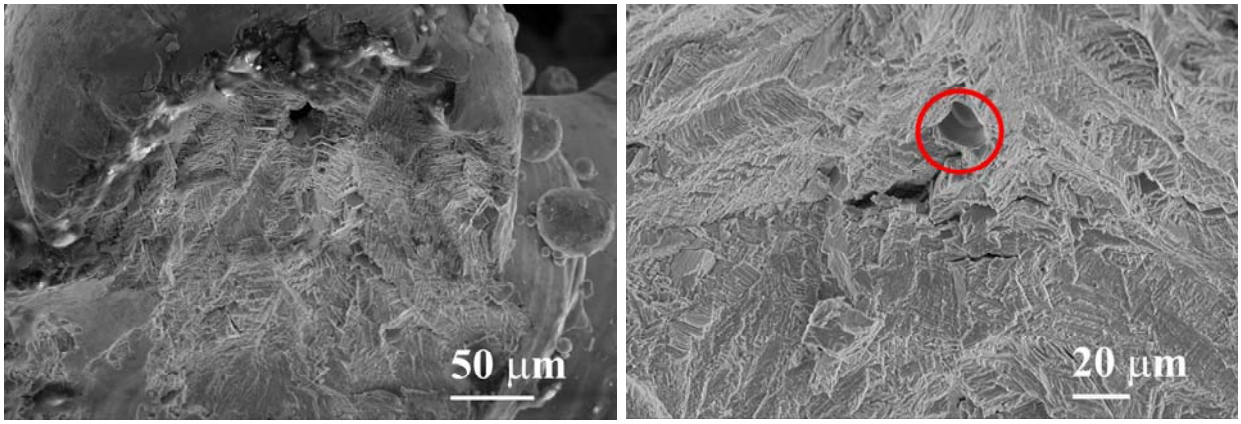

(a)

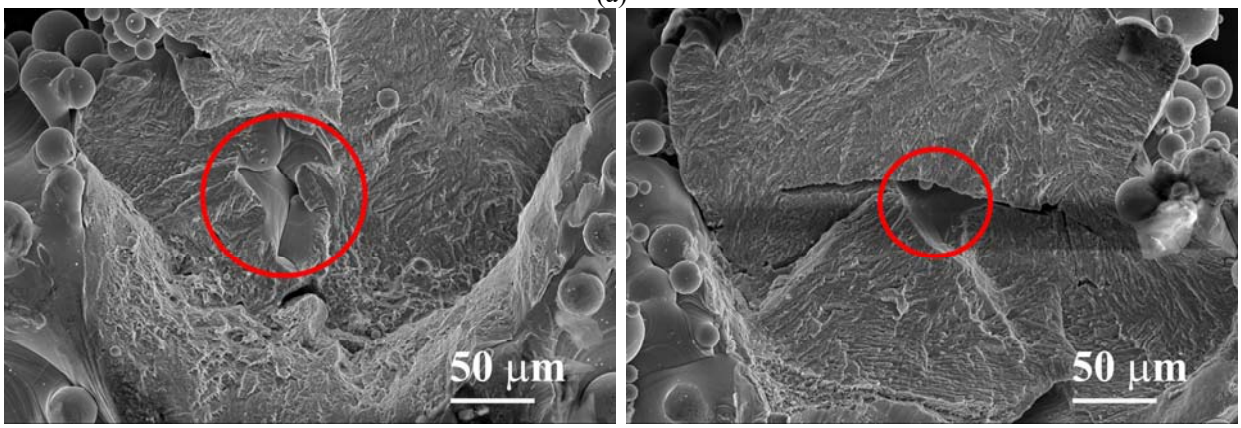

(b)

Figure 5- Manufacturing defects in the struts of selective laser melted (a) Co-Cr and (b) Ti-6Al-4V porous structures

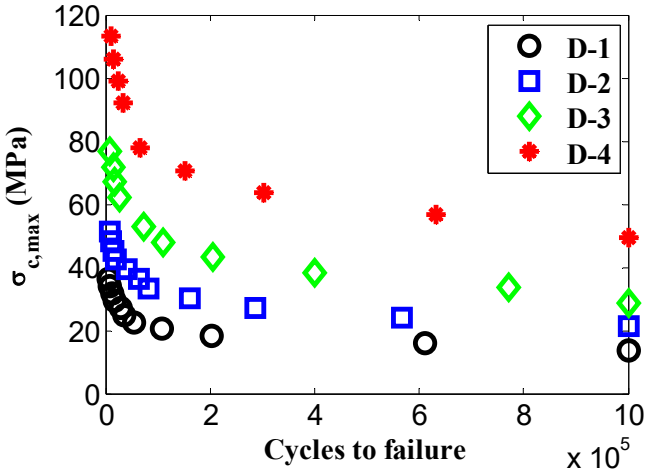

(a)

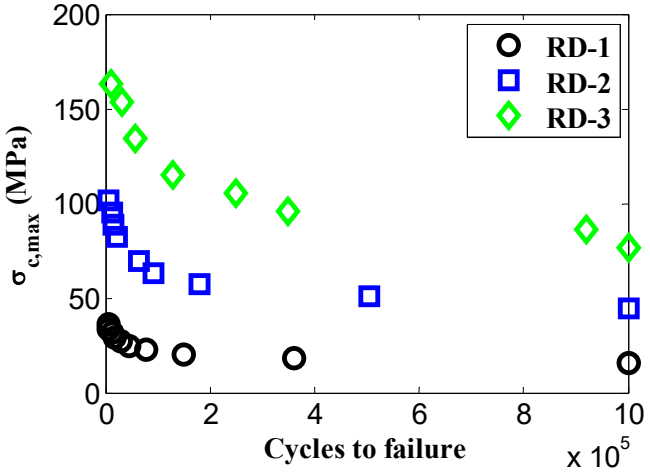

(b)

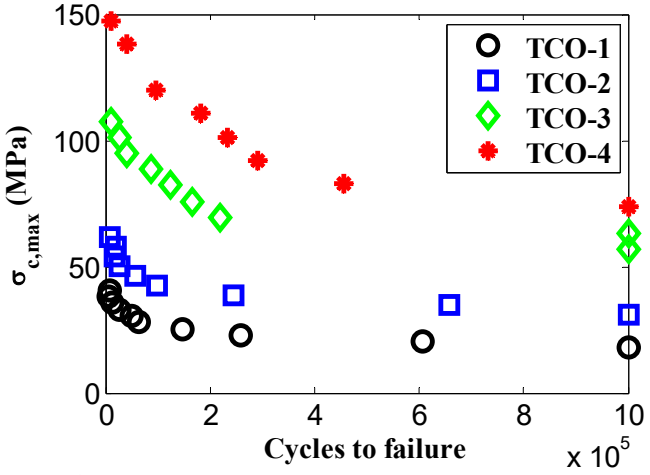

(c)

Figure 6- S-N curves of Co-Cr porous structures based on (a) diamond, (b) rhombic dodecahedron, and (c) truncated cuboctahedron unit cells ($\sigma_{c,max}$ stands for maximum compressive stress, i.e. minimum stress, in each loading cycle)

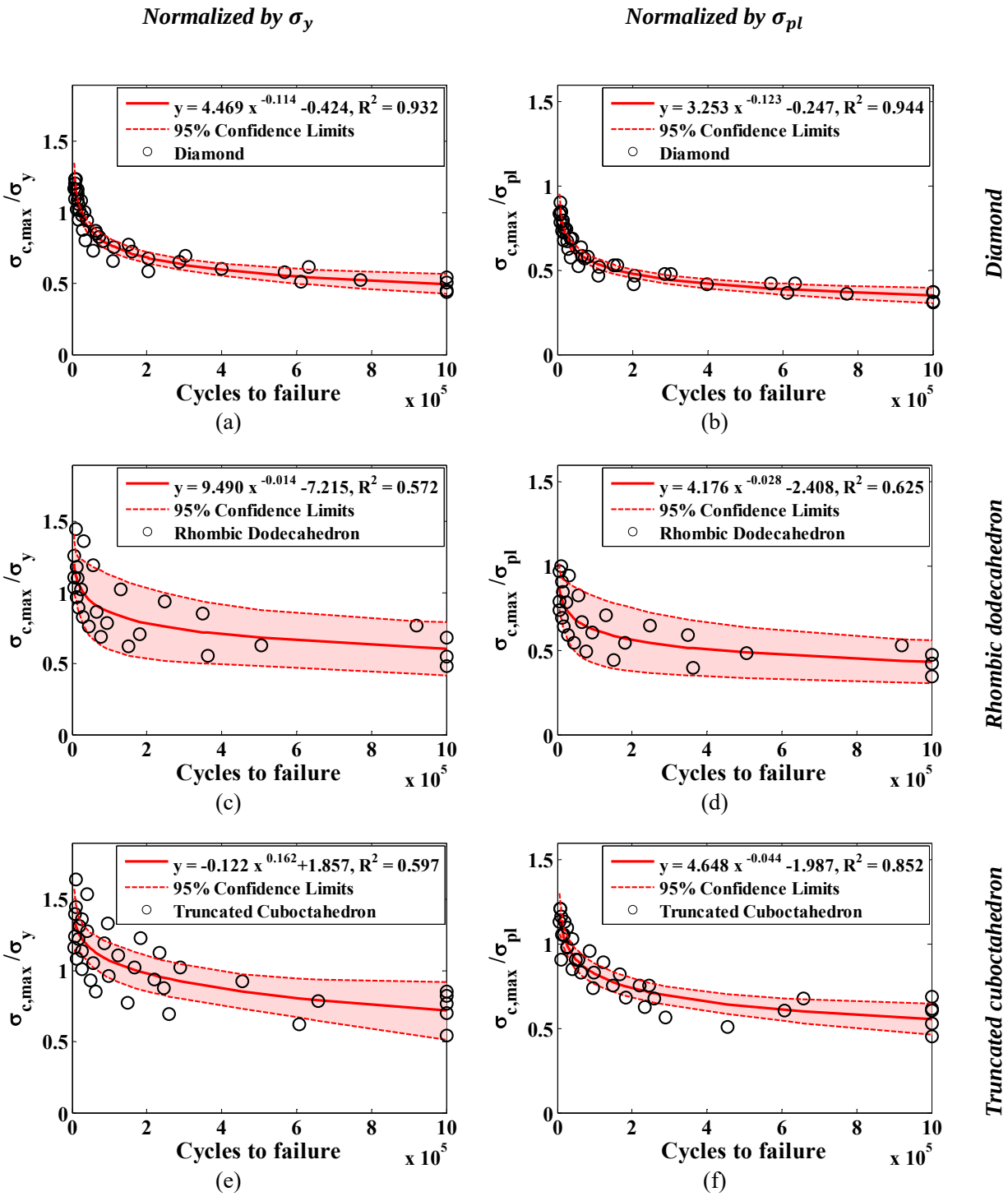

Figure 7- Normalized S-N curves of Co-Cr porous structures based on diamond, rhombic dodecahedron, and truncated cuboctahedron unit cells. In equations presented in each graph, y represents the vertical axis parameter (i.e. $\sigma_{c,max}/\sigma_x$) and x represents the horizontal parameter (i.e. number of cycles to failure). R^2 represents the coefficient of determination for the simple linear regression method used for fitting the curves to the data.

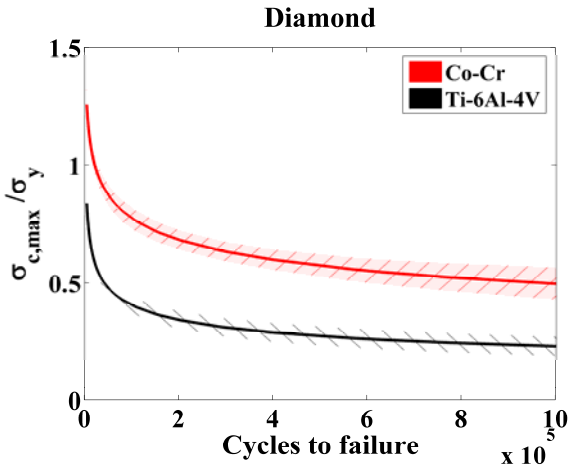

(a)

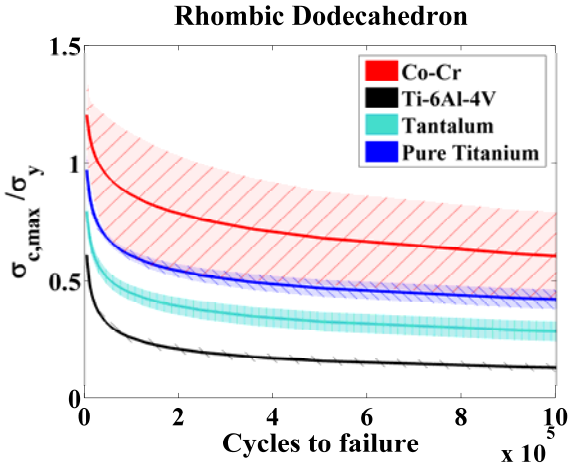

(b)

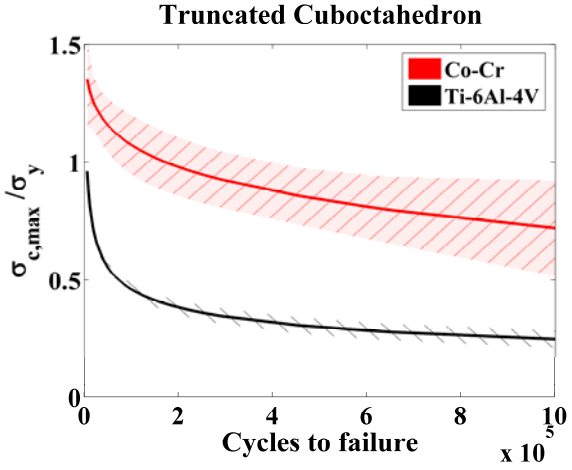

(c)

Figure 8- Comparison of normalized S-N curves of porous structures made from Co-Cr, Ti-6Al-4V, tantalum, and commercially pure titanium based on (a) diamond, (b) rhombic dodecahedron, and (c) truncated cuboctahedron unit cells

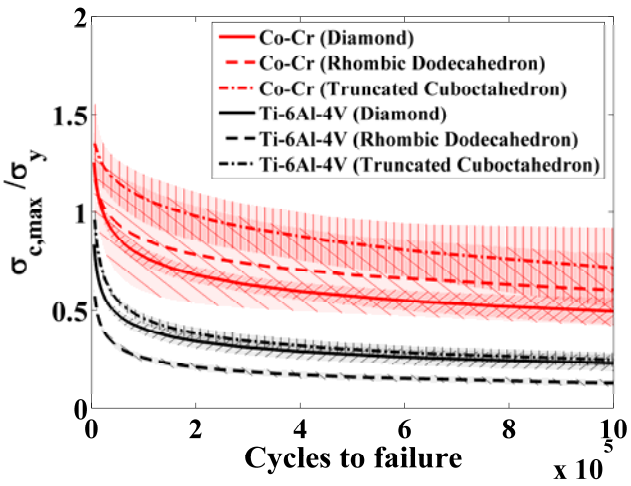

Figure 9- Comparison of normalized S-N curves of Co-Cr porous structures based on different unit cell types

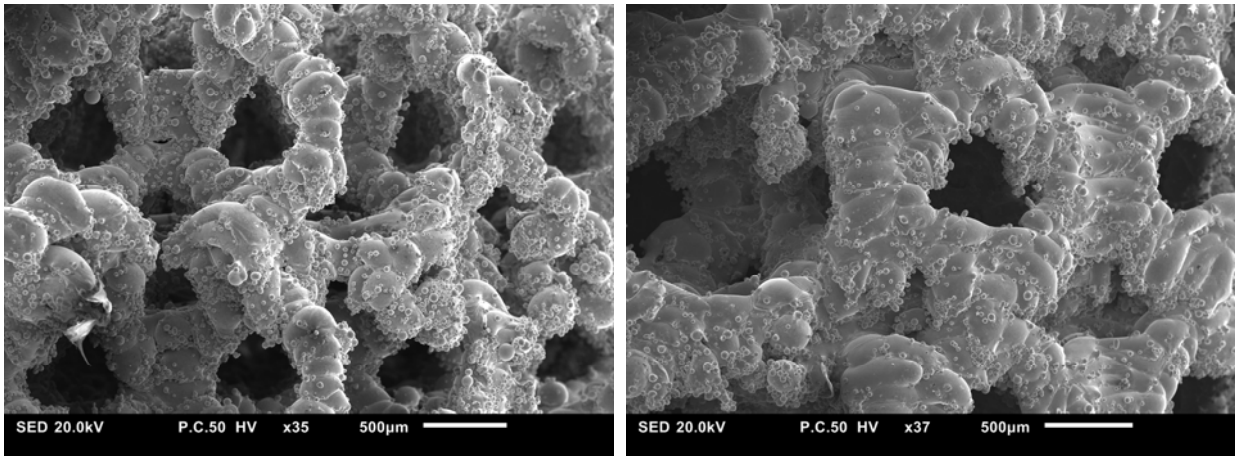

(a) (b)

Figure 10- Morphology of Co-Cr porous structures based on truncated cuboctahedron unit cell with relative densities of 0.236 (TCO-1) and (b) 0.386 (TCO-4).